EDGE ARTICLE

Stimulating the Lewis acidity of Pt–O–Co bridges *via* vacancy engineering for efficient hydrogen evolution in seawater

Mengyue Gao,[a] Junfeng Qin,*[b] Rui Zhang,[ac] Xu Liu,[ac] Yuxin Liu,[ac] Yuxin Zhang,[ac] Long Song,[a] Jingyi Xie,[d] Jingqi Chi,[ID] *[a] Xiaobin Liu*[ac] and Lei Wang[ID] *[a]

Seawater electrolysis is considered a promising approach for large scale sustainable hydrogen production. However, its complex ionic environment often causes precipitation formation and Cl^- poisoning of active sites, severely hindering the hydrogen evolution reaction (HER) kinetics. Here, we construct a low-Pt-doped and vacancy-rich cobalt oxide catalyst ($Pt–CoO_x$), in which vacancy rich asymmetric Pt–O–Co bridge structure induces charge polarization and strengthens the Lewis acidity of Co sites, thereby enabling selective OH^- adsorption while suppressing chloride ion (Cl^-) adsorption and effectively preventing poisoning of the Pt active centers. *In situ* characterization and theoretical calculations reveal that the asymmetric Pt–O–Co bridge with rich O vacancies achieves ideal hydrogen adsorption energetics and disrupts the hydrogen bond network of interfacial water molecules, thereby lowering the energy barrier for water dissociation and preventing the formation of precipitates. Benefiting from above, $Pt–CoO_x$ requires only 160.22 mV to deliver 500 mA cm^{-2} in alkaline seawater and maintains excellent durability in natural seawater. When integrated into an anion exchange membrane water electrolyzer (AEMWE), the catalyst achieves an industrial level current density of 1 A cm^{-2} at 1.97 V and operates stably for more than 100 hours at 500 mA cm^{-2}.

Introduction

With the growing global energy crisis and environmental concerns, water electrolysis driven by renewable energy has been recognized as one of the most promising strategies for achieving a zero carbon energy economy.[1,2] However, the scarcity of freshwater resources limits the large scale deployment of traditional alkaline electrolysis.[3,4] In this context, seawater, due to its abundance and low cost, has emerged as an attractive alternative electrolyte. Nevertheless, the complex ionic composition of seawater introduces new challenges. During the cathodic process, hydroxide ions (OH^-) generated and accumulated on the catalyst surface occupy active sites and hinder the adsorption of reactant species. In addition, excessive local OH^- concentration promotes the precipitation of Ca^{2+} and Mg^{2+}

species, while chloride ions (Cl^-) can cause surface poisoning and structural corrosion.[5,6] These processes block active sites, hinder charge transfer, and lead to catalyst deactivation, resulting in much slower HER kinetics than in pure alkaline electrolytes.[7,8]

Platinum based catalysts possess nearly ideal hydrogen adsorption free energy and thus exhibit outstanding intrinsic HER activity.[9,10] However, their superior performance generally requires a high noble metal loading, which significantly increases cost and limits large scale application.[11,12] In addition, conventional Pt catalysts suffer from three intrinsic problems: sluggish water dissociation, susceptibility to OH^- and Cl^- poisoning, and surface blockage by Ca^{2+} or Mg^{2+} deposits in seawater.[13] These issues severely restrict their practical use. Therefore, developing low Pt catalysts with high activity and durability that can promote water dissociation and resist hydroxide adsorption and salt deposition remains a key scientific challenge. Recent studies have demonstrated that constructing asymmetric metal oxygen bridges ($M_1–O–M_2$) can effectively modulate interfacial charge transfer and accelerate key steps in the HER, thereby improving catalytic performance. For example, Yang *et al.* introduced Mn atoms into RuO_2 to form locally asymmetric Mn–O–Ru bridges, where the synergistic effect between Mn and Ru sites enhanced both water dissociation and hydrogen adsorption.[14] Such asymmetric bridge structures can tune electronic coupling between metal

[a]*Key Laboratory of Eco-Chemical Engineering, International Science and Technology Cooperation Base of Eco-Chemical Engineering and Green Manufacturing, College of Chemical Engineering, Qingdao University of Science and Technology, Qingdao 266042, PR China. E-mail: chijingqi@qust.edu.cn; liuxb@qust.edu.cn; inorchemwl@126.com*

[b]*Hunan Provincial Key Laboratory of Water Treatment Functional Materials, College of Chemistry and Materials Engineering, Hunan University of Arts and Science, Changde 415000, Hunan, People's Republic of China. E-mail: qinjunfeng@huas.edu.cn*

[c]*College of Environment and Safety Engineering, Qingdao University of Science and Technology, Qingdao 266042, PR China*

[d]*Key Laboratory of Materials and Surface Technology (Ministry of Education), School of Materials Science and Engineering, Xihua University, Chengdu, 610039, China*

centers and optimize the binding of reaction intermediates. Furthermore, during the HER process, excessive OH^- adsorption on active sites often leads to catalyst poisoning, which suppresses the adsorption of reactant species and, in seawater electrolytes, further accelerates the formation of insoluble precipitates. Introducing Lewis acidic sites within asymmetric bridges can preferentially bind OH^- and prevent its accumulation on active centers. According to the hard soft acid base (HSAB) theory, Lewis acid sites strongly interact with basic OH^- species, thereby mitigating active site poisoning.[15,16] Therefore, regulating the Lewis acidity of these bridge sites to enhance the

adsorption of OH^- is crucial for preventing deactivation of active sites and improving HER kinetics but has been barely reported and remains challenging.

To address these challenges, we developed a low-Pt-doped, vacancy-rich cobalt oxide catalyst ($Pt–CoO_x$) featuring an asymmetric Pt–O–Co bridge structure. The introduction of vacancies alters the electronic configuration of the metal centers, promotes electron transfer of Pt–O–Co bridges, enriches Pt with electrons, and enhances the Lewis acidity of Co sites. The strengthened Lewis acid centers preferentially adsorb OH^-, thus preventing its accumulation on Pt and avoiding
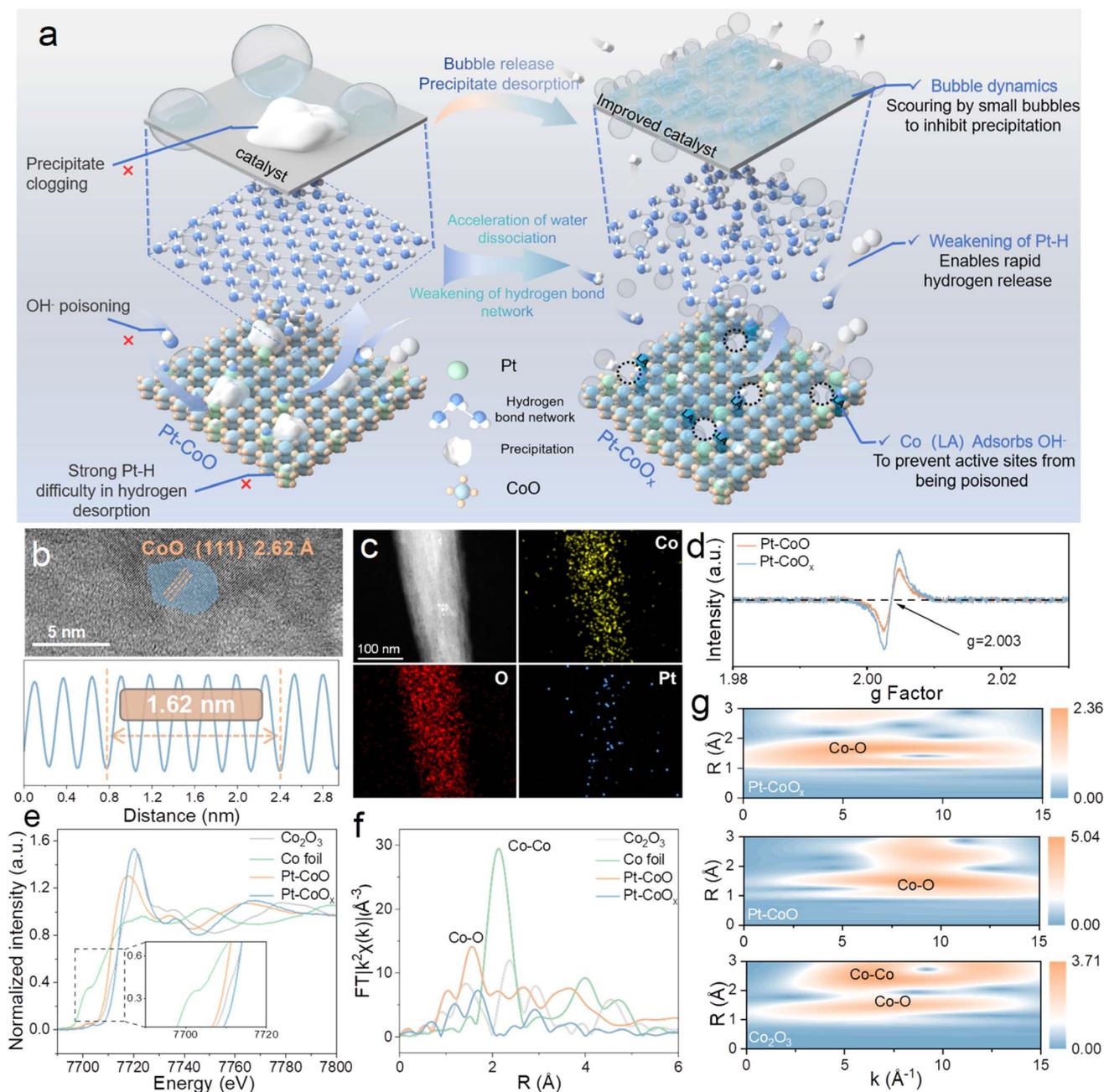

Fig. 1   (a) Mechanistic illustration of $Pt–CoO_x$ and $Pt–CoO$ catalysts. (b) HRTEM of $Pt–CoO_x$. (c) EDX elemental maps. (d) EPR spectra. (e) Co K-edge XANES spectra. (f) Fourier transformed EXAFS spectra, and (g) WT contour plots of Co K-edge EXAFS for $Pt–CoO_x$, $Pt–CoO$, and reference samples.

poisoning of active sites. Importantly, the formation of vacancies disrupts the hydrogen bond network of interfacial water, increases the proportion of free water, and facilitates rapid bubble detachment. This dynamic surface environment effectively suppresses Ca/Mg^{2+} precipitation and prevents site blockage (Fig. 1a). Benefiting from these synergistic effects, Pt–CoO_x exhibits excellent resistance to poisoning, deposition, and corrosion in alkaline seawater, achieving a high current density of 500 mA cm^{-2} at an overpotential of only 160.22 mV and maintaining structural and electrochemical stability during long term operation. When employed as the cathode in an anion exchange membrane seawater electrolyzer, Pt–CoO_x operates stably for over 100 hours at 0.5 A cm^{-2} with negligible degradation, demonstrating superior catalytic activity and durability.

Catalyst synthesis and characterization

The oxygen vacancy rich platinum doped cobalt oxide catalyst (Pt–CoO_x) was synthesized on nickel foam using a two-step method. First, a CoO precursor was obtained through a hydrothermal reaction, followed by $NaBH_4$ reduction and H_2PtCl_6 impregnation to introduce Pt species and generate oxygen vacancies (Fig. S1). Scanning electron microscopy (SEM) images reveal that the CoO precursor is uniformly grown on the substrate, forming dense short needle like structures (Fig. S2). After subsequent treatment, Pt–CoO_x and Pt–CoO maintain similar morphologies to that of pristine CoO (Fig. S3 and S4), indicating that Pt doping and vacancy formation do not alter the overall structure. This short needle like morphology favors a larger specific surface area and exposes more active sites. High resolution transmission electron microscopy (HRTEM) further confirms a lattice spacing of 2.62 Å, corresponding to the (111) plane of CoO, verifying the successful formation of the CoO structure (Fig. 1b).[17] Typical TEM and elemental mapping images show uniform distributions of Co, O, and Pt elements in Pt–CoO_x (Fig. 1c), consistent with the corresponding energy dispersive X-ray spectroscopy (EDX) results (Fig. S5). X-ray diffraction (XRD) patterns (Fig. S6) display characteristic diffraction peaks indexed to CoO (PDF#42-1300) and the Ni substrate (PDF#04-0950), while no distinct Pt related peaks are observed, suggesting that Pt exists in a highly dispersed or low content state rather than forming a separate metallic phase, consistent with the TEM observations. Inductively coupled plasma optical emission spectrometry (ICP-OES) analysis determines a Pt content of only 3.44 wt% (Table S1), which is significantly lower than that of commercial Pt/C catalysts. Raman spectra (Fig. S7) show the characteristic Co–O vibration modes at approximately 190, 473, 515, 602, and 657 cm^{-1}, in line with typical cobalt oxides.[18] Electron paramagnetic resonance (EPR) spectra (Fig. 1d) further confirm the presence of oxygen vacancies. Pt–CoO_x exhibits a strong signal at $g = 2.003$, suggesting an increased concentration of unpaired electrons induced by vacancy formation.[19] X-ray photoelectron spectroscopy (XPS) survey spectra (Fig. S8) confirm the presence of Co, Pt, and O elements in the samples. The high resolution O 1s spectrum (Fig. S9) can be deconvoluted into three peaks located

at 532.8, 531.7, and 530.7 eV, corresponding to adsorbed water, oxygen vacancies, and lattice oxygen, respectively.[20] Notably, Pt–CoO_x exhibits a significantly larger peak area associated with oxygen vacancies compared with Pt–CoO, which is consistent with the EPR results. The introduction of oxygen vacancies not only creates more coordinatively unsaturated reactive sites but also enhances the charge transport capability of the material, synergistically facilitating the electrocatalytic process. The Pt 4f spectrum (Fig. S10) confirms the successful incorporation of Pt, displaying Pt^0 and Pt^{2+} signals at approximately 70.3 and 71.0 eV, respectively.[21] Quantitative analysis shows that the Pt^0/Pt^{2+} ratio in Pt–CoO_x is higher than that in Pt–CoO, indicating that the presence of oxygen vacancies promotes the reduction of Pt species. The high resolution Co 2p spectra (Fig. S11) of both samples display characteristic Co $2p_{3/2}$ and Co $2p_{1/2}$ doublets along with satellite peaks. Compared with Pt–CoO, the Co 2p binding energies of Pt–CoO_x shift positively, accompanied by an increase in Co^{3+} signals and a decrease in Co^{2+} signals. This suggests that Pt doping and oxygen vacancy formation decrease the electron density of Co, leading to a higher oxidation state. Such behavior can be attributed to strong electronic coupling interactions along the Pt–O–Co bridge bonds. To further investigate the local chemical environment and electronic structure, the Co K-edge X-ray absorption near-edge structure (XANES) spectrum (Fig. 1e) shows a pronounced positive shift for Pt–CoO_x compared with Pt–CoO, indicating an elevated average Co oxidation state. Quantitative analysis of the absorption edge energy reveals (Fig. S12) that the average Co valence in Pt–CoO_x is approximately +3.27, significantly higher than that in Pt–CoO (+2.18), in good agreement with the XPS results and further confirming the oxygen-vacancy-induced oxidation of Co sites. The Fourier transformed EXAFS spectra (Fig. 1f) reveal that introducing oxygen vacancies disrupts the local Co–O coordination environment, indicating an increase in coordination incompleteness around cobalt sites. A noticeable shift of the Co–O peak toward higher R values further suggests an elongation of the Co–O bond distance. Such a change in bond length also drives a rearrangement of the original Co–O–Co bridging framework.[22] Once part of the bridging oxygen is removed, the nearby Co centers undergo redistribution of their coordination electrons, reflecting vacancy induced electronic reorganization that strengthens the Co–O interaction. This reconstruction of the bridging network facilitates the emergence of a new Pt–O–Co linkage at the metal oxide interface, thereby establishing an efficient pathway for interfacial electronic coupling. Moreover, the wavelet transform (WT) analysis (Fig. 1g) demonstrates that Pt–CoO_x and Pt–CoO exhibit similar coordination features, however, the signal of Pt–CoO_x is more dispersed, suggesting that the generation of oxygen vacancies disrupts the local symmetry and significantly modulates the electronic structure.[23] Among them, Co foil and Co_2O_3 serve as standard reference materials. Overall, the synergistic introduction of Pt and oxygen vacancies preserves the morphological and structural integrity of the material while reconstructing the Pt–O–Co bridge bonds. This structural rearrangement reshapes the Co valence distribution, enhances the Lewis acidity of Co

sites, and establishes an optimized electronic structure favorable for accelerating the HER kinetics.[24,25]

Electrocatalytic performance evaluation

The electrocatalytic performance of Pt–CoO$_x$ was systematically evaluated in both 1.0 M KOH and alkaline seawater electrolytes. As shown in Fig. S13, Pt–CoO$_x$ exhibits significantly enhanced HER activity compared with the reference samples. In 1.0 M KOH, Pt–CoO$_x$ requires overpotentials of only 133 and 177 mV to reach current densities of 500 and 1000 mA cm^{-2}, respectively, which are markedly lower than those of Pt–CoO (164 and 217 mV) and CoO (410.02 and 452.52 mV). In addition, Pt–CoO$_x$ shows a much smaller Tafel slope of 39.67 mV dec^{-1} and a lower charge transfer resistance of 1.285 Ω compared with Pt–CoO, indicating faster reaction kinetics. These results confirm that the introduction of oxygen vacancies significantly enhances the intrinsic catalytic activity of the catalyst. Given the outstanding performance of Pt–CoO$_x$ in alkaline medium, its electrocatalytic behavior was further examined in alkaline seawater to evaluate its feasibility for large scale hydrogen production. As shown in the linear sweep voltammetry (LSV) curves (Fig. 2a), Pt–CoO$_x$ maintains excellent HER activity in alkaline seawater, requiring overpotentials of only 160.22 and 207.22 mV to achieve 500 and 1000 mA cm^{-2}, respectively, which are notably lower than those of the control samples (Fig. S14). Kinetic analyses (Fig. 2b) further demonstrate that Pt–CoO$_x$ exhibits the lowest Tafel slope and the smallest interfacial charge transfer resistance, along with a larger electrochemical double layer capacitance and a higher turnover frequency (Fig. S15–S17). These results suggest that Pt–CoO$_x$ possesses highly efficient charge and proton transfer capabilities and fully utilizes its active sites, leading to superior HER kinetics. Its overall performance also surpasses that of most recently reported cobalt based HER catalysts (Fig. 2c). Stability is another crucial factor for evaluating seawater electrolysis catalysts. As shown in Fig. S18, Pt–CoO$_x$ maintains nearly constant potential during continuous operation at a current density of 100 mA cm^{-2} for 20 hours in alkaline seawater, exhibiting remarkable durability. Furthermore, the SEM images (Fig. S19) and XPS analyses (Fig. S20) obtained after the stability test show no obvious changes, indicating that no significant surface reconstruction or compositional evolution of the catalyst occurs during long term operation. To further verify its practical potential, an anion exchange membrane water electrolyzer (AEMWE) was assembled using Pt–CoO$_x$ as the cathode and S-(Ni,Fe)OOH as the anode, and operated in alkaline seawater at 75 °C. As shown in Fig. 2d, the S-(Ni,Fe)OOH∥Pt–CoO$_x$ electrolyzer demonstrates excellent overall water electrolysis performance, requiring only 1.97 V to deliver an industrially relevant current density of 1.0 A cm^{-2} (Fig. 2e), which is substantially lower than that of the S-(Ni,Fe)OOH∥Pt/C system. At a current density of 400 mA cm^{-2}, the operating voltage of the S-(Ni,Fe)OOH∥Pt–CoO$_x$ system is
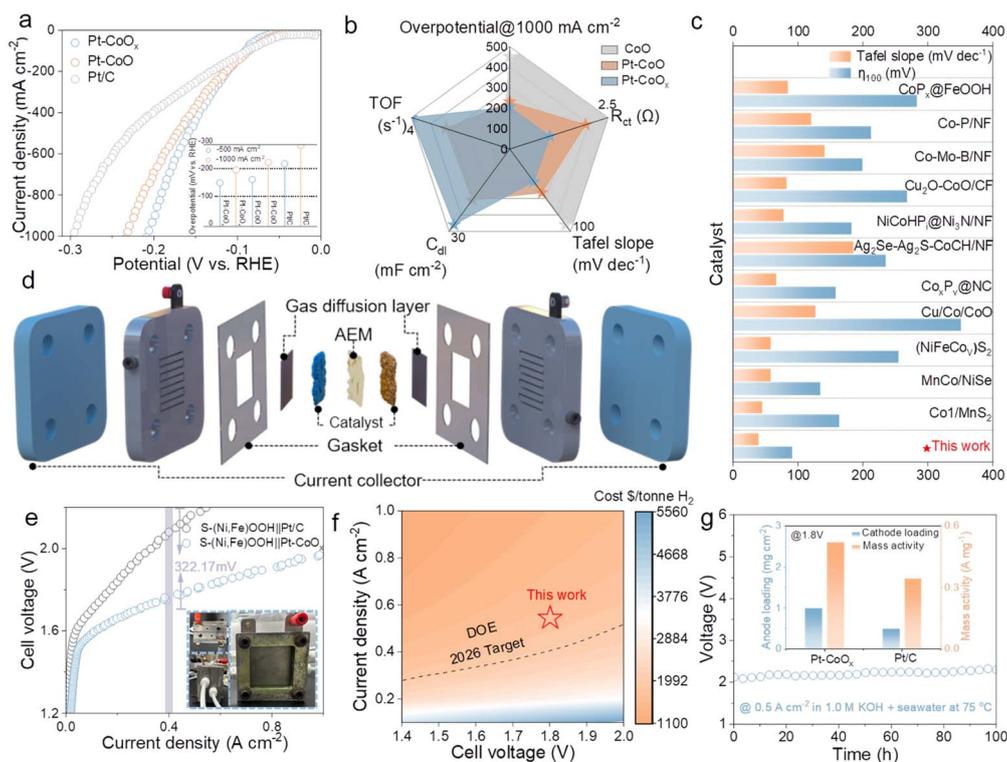

Fig. 2 (a) LSV curves in 1.0 M KOH + seawater electrolyte. (b) Radar chart of kinetic parameters. (c) Comparison of overpotentials and Tafel slopes with reported HER catalysts. (d) Schematic diagram of the AEMWE configuration. (e) Polarization curves of AEMWE with different electrodes. (f) Cost analysis of hydrogen production as a function of electrolyzer cell voltage and operating current density. (g) Stability test and mass activity of catalysts.

322.17 mV lower than that of the S-(Ni,Fe)OOH‖Pt/C configuration, demonstrating its clear superiority and strong potential for large scale applications. Based on the current density range of $0–1.0$ A cm^{-2} (Fig. S21), the hydrogen production efficiency of the system is maintained between 60% and 85%, with low energy consumption. Based on the experimental results, a detailed techno economic analysis (TEA) was performed to evaluate the overall cost of hydrogen production. The total cost mainly consists of electricity, electrolyzer units, catalysts, membrane materials, installation and balance of plant (BOP) systems, chemical reagents, and operating expenses.[26] The analysis indicates that electricity represents the major cost contributor. Under the condition of a 1 mol KOH plus seawater electrolyte, the system operates steadily at 500 mA cm^{-2} and 1.8 V (Fig. 2f and S22), corresponding to a hydrogen production cost of 1817.42 USD per ton, which is already below the 2000 USD per ton target set by the U.S. Department of Energy for

2026. Further cost reductions can be achieved by lowering the catalytic voltage and adopting low cost electricity sources. The S-(Ni,Fe)OOH‖Pt–CoO$_x$ electrolyzer also exhibits outstanding long term operational stability, continuously running for more than 100 hours at 500 mA cm^{-2} without any noticeable voltage decay (Fig. 2g). At the same time, its stability performance is superior compared with the data reported in the literature as summarized in Table S3. Impressively, the inset shows that Pt–CoO$_x$ (1.0 mg cm^{-2}) delivers a higher mass activity than commercial Pt/C (0.5 mg cm^{-2}), indicating a significantly improved noble metal utilization efficiency.[27] Furthermore, to evaluate the faradaic efficiency of seawater electrolysis, the amount of hydrogen evolved was quantitatively measured using the setup illustrated in Fig. S23. The results reveal that at a current density of 100 mA cm^{-2}, the measured faradaic efficiency approaches 100%, and the experimentally determined hydrogen production rate is nearly identical to the theoretical
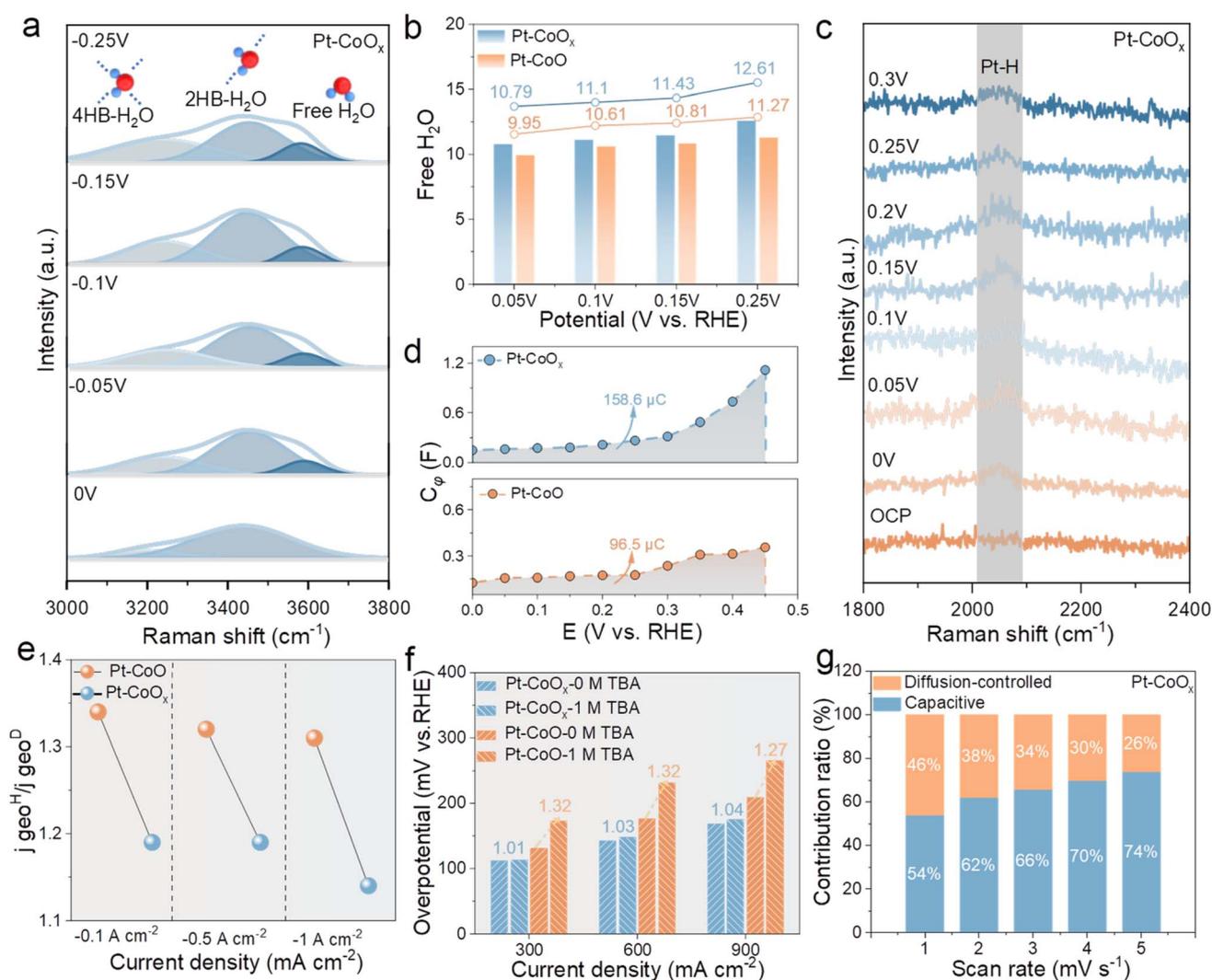

Fig. 3 (a) In situ Raman spectra of interfacial water at the Pt–CoO$_x$ interface. (b) The proportion of free water on the catalyst surface at different potentials. (c) In situ Raman spectra of Pt–CoO$_x$ in 1.0 M KOH + seawater at different potentials. (d) Comparison of the C_φ-overpotential dependence for Pt–CoO$_x$ and Pt–CoO. (e) KIE values at corresponding potentials. (f) Comparison of overpotentials with different concentrations of TBA. (g) Pt–CoO$_x$ contribution rate of pseudocapacitance derived from the CV curve calculation.

value. This finding confirms that almost all electrons are efficiently converted into hydrogen without noticeable side reactions.[28]

Mechanistic insights into the enhanced HER activity

To unravel the intrinsic origin of the enhanced hydrogen evolution performance of Pt–CoO$_x$, *in situ* Raman spectroscopy was employed to monitor the adsorption and dissociation of H$_2$O during electrolysis. Spectra of Pt–CoO$_x$ and Pt–CoO were recorded at various potentials in alkaline seawater (Fig. 3a and S24). The broad band observed between 3000 and 3800 cm^{-1} corresponds to the O–H stretching vibrations of interfacial water and can be deconvoluted into three Gaussian components: the peaks at 3200, 3400, and 3600 cm^{-1} arise from tetra hydrogen bonded water (4HB), double hydrogen bonded water (2HB), and non-hydrogen bonded or free water molecules (free H$_2$O).[29,30] As shown in Fig. 3b, the fraction of free water on Pt–CoO$_x$ increases from 10.79% to about 12.61% with increasing potential, suggesting a gradual disruption of the hydrogen bond network. In contrast, Pt–CoO exhibits a lower proportion of free water, implying that the Pt–O–Co bridge with rich O vacancies enhances interfacial water polarization and thus facilitates water activation and dissociation. These results further verify that oxygen vacancy induced charge redistribution increases the Lewis acidity of Co sites, which in turn attracts the lone pair electrons of nearby water molecules and promotes their dissociation on the Pt–CoO$_x$ surface. As shown in Fig. 3c and S24, the Pt–H vibration intensity of Pt–CoO$_x$ first increases and then declines with rising potential, remaining consistently weaker than that of Pt–CoO. This behavior indicates that the electronic reconstruction induced by oxygen vacancies weakens the Pt–H bond, leading to a more balanced hydrogen adsorption desorption process and improved HER kinetics.[31,32] *In situ* electrochemical impedance spectroscopy (EIS) measurements were further performed (Fig. S25). By fitting the charge transfer resistance (R_{ct}) and the pseudocapacitance associated with hydrogen adsorption (C_φ), the adsorption behavior of H* intermediates was evaluated. Integration of C_φ yields the corresponding hydrogen adsorption charge (Q_{H*}) (Fig. 3d). Pt–CoO$_x$ shows a markedly higher Q_{H*} than Pt–CoO, indicating a higher surface hydrogen coverage (θ_H). In the log(R_{ct}) overpotential plots (Fig. S26), the smaller slope of Pt–CoO$_x$ suggests faster H* adsorption desorption dynamics.[33–35] The Bode plots (Fig. S27) reveal that low frequency regions mainly reflect charge transfer at the electrolyte catalyst interface, whereas the high frequency regions correspond to electron migration within the catalyst. The minor phase angle variation at high frequencies and the pronounced change at low frequencies indicate that charge transfer resistance during the HER primarily originates from the electrolyte catalyst interface. Compared with Pt–CoO, Pt–CoO$_x$ exhibits a faster decay of low frequency peaks with increasing overpotential, confirming that the Pt–O–Co bridge substantially promotes interfacial charge transfer and accelerates HER kinetics. To examine the rate determining step of the HER, kinetic isotope effect (KIE) measurements were conducted in 1.0 M KOD + D$_2$O electrolyte. As shown in Fig. S28, both

catalysts display reduced activity in D$_2$O, but the relatively high KIE values indicate that hydrogen transfer is the key rate limiting process. Notably, Pt–CoO$_x$ exhibits a lower KIE value than Pt–CoO (Fig. 3e), implying more favorable hydrogen transfer kinetics.[14] The stability of surface active H* species was further examined using *tert* butanol (TBA) as a radical scavenger (Fig. S29).[36] In 1.0 M KOH containing TBA, the HER activity of both catalysts slightly decreased. As shown in Fig. 3f, Pt–CoO$_x$ exhibited the smallest attenuation at current densities of 300, 600, and 900 mA cm^{-2}, with values of 1.01, 1.03, and 1.04, respectively, indicating a high H* coverage on the surface. These H* species are resistant to TBA removal, reflecting its accelerated water dissociation kinetics and the generation of more adsorbed hydrogen. Finally, cyclic voltammetry in the non-faradaic potential region was employed to assess the pseudocapacitive characteristics of the catalysts. As shown in Fig. 3g and S30–S32, Pt–CoO$_x$ exhibits a significantly higher pseudocapacitance, suggesting that the asymmetric Pt–O–Co bridging structure with rich oxygen vacancies enhances electronic conductivity and charge storage capacity, thereby synergistically contributing to its superior HER performance.

DFT calculation

To gain deeper insight into the origin of the enhanced HER activity of Pt–CoO$_x$, density functional theory (DFT) calculations were carried out based on the experimentally derived structural models of Pt–CoO$_x$ and Pt–CoO (Fig. S33). The differential charge density maps reveal pronounced charge redistribution among Pt, Co, and O atoms (Fig. 4a), with yellow and blue regions representing charge accumulation and depletion, respectively.[37] Formation of oxygen vacancies generates localized electron deficient regions around the missing oxygen sites. Simultaneously, adjacent Co atoms undergo partial electron loss, which in turn increases the electron density on neighboring Pt atoms, consistent with XPS and XANES observations. The bridging oxygen atoms act as electronic mediators, enabling partial charge transfer from Co to Pt and stabilizing the local electronic environment. Local charge density maps (Fig. 4b and S34) further corroborate the distinct redistribution of surface electrons before and after vacancy formation. Density of states (DOS) analysis (Fig. 4c and d) reveals that the asymmetric Pt–O–Co bridging unit with rich oxygen vacancies significantly tunes the electronic configuration of Pt–CoO$_x$. Compared with Pt–CoO, the total DOS of Pt–CoO$_x$ exhibits a narrower distribution, suggesting a transition from delocalized to more localized electronic states due to lattice distortion.[38] Projected DOS (PDOS) results (Fig. S35) further show that oxygen vacancy formation reduces the coordination number of Pt, leading to a shift of Pt states toward the Fermi level.[39] This indicates increased surface electron density on Pt, which modulates its interaction with hydrogen intermediates. To further clarify the catalytic role of the Pt–O–Co bridge in the HER process, the energy barrier for water dissociation was calculated (Fig. 4e and S36). The barrier on Pt–CoO$_x$ is lower than that on Pt–CoO, indicating more favorable H$_2$O activation and confirming that the Pt–O–Co bridge effectively facilitates
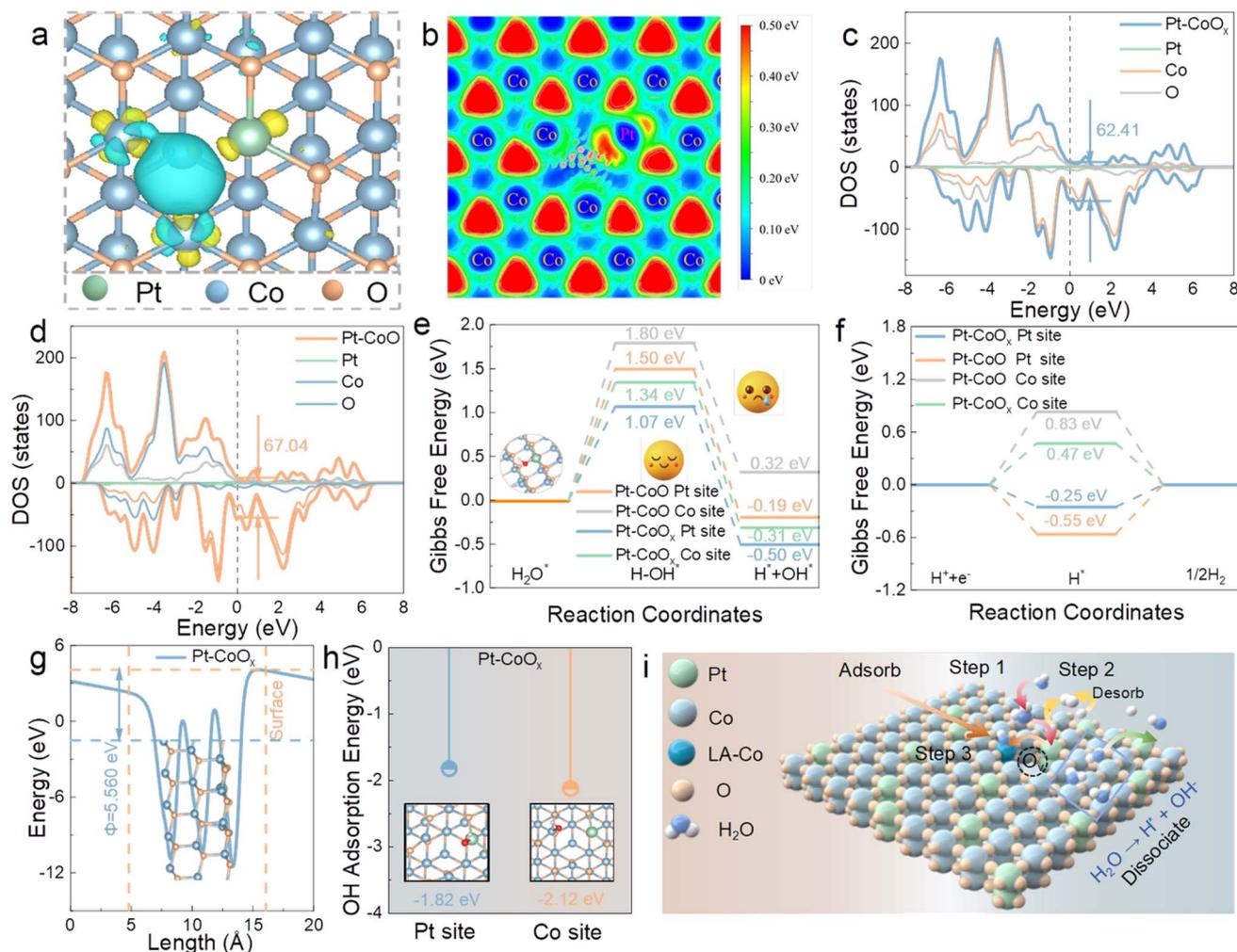
Fig. 4 (a) Charge density difference of Pt−CoO$_x$. (b) Electron locational function plot for Pt−CoO$_x$. Density of states (DOS) of (c) Pt−CoO$_x$ and (d) Pt−CoO. (e) Calculation results of hydrogen adsorption free energy at different sites. (f) Energy distribution of water molecule dissociation on Pt−CoO$_x$ and Pt−CoO surfaces. (g) Work function of Pt−CoO$_x$. (h) OH$^-$ adsorption energy at different sites in Pt−CoO$_x$. (i) Schematic diagram of possible HER reaction pathways on Pt−CoO$_x$.

water dissociation, thereby creating active sites for subsequent hydrogen generation. The free energy of hydrogen adsorption (ΔG_{H*}) on the Pt−O−Co bridge (Fig. 4f and S37) shows that the Pt sites in Pt−CoO$_x$ are close to thermoneutral, exhibiting more balanced hydrogen adsorption desorption behavior than Co sites.[40] Work function analysis (Fig. 4g and S38) further reveals a slight reduction for Pt−CoO$_x$ relative to Pt−CoO, implying enhanced electron migration from the bulk to the surface due to under coordinated Pt/Co atoms. Under alkaline conditions, strong OH$^-$ adsorption poisons Pt sites and hinders HER kinetics. In Pt−CoO$_x$, electron redistribution regulated by oxygen vacancies aggravates the asymmetric evolution of Pt−O−Co bridge oxygen structures, increasing the Lewis acidity of Co centers. Co atoms act as Lewis acidic centers, preferentially binding OH$^-$ and facilitating hydrogen exfoliation from Pt to Co (Fig. 4h). This reduces OH$^-$ coverage on Pt, preventing site deactivation. Overall, the introduction of oxygen vacancies significantly optimizes the hydrogen desorption free energy (Fig. 4i). Based on the above analysis, we speculate the following

reaction pathway. First, water molecules are adsorbed on Pt sites near oxygen vacancies, facilitating initial hydrogen activation (Path 1). Next, hydrogen atoms desorb from the Pt sites to form H$_2$ (Path 2). Finally, the resulting hydroxyl (OH$^-$) species preferentially migrate to Lewis acidic Co centers, alleviating surface poisoning of Pt (Path 3). These synergistic processes collectively regulate interfacial reaction kinetics, enhance catalyst stability, and ultimately enable the Pt−Co oxide system to achieve superior hydrogen evolution activity and durability.

Electrochemical properties of natural seawater

Theoretical analysis reveals that oxygen vacancies markedly enhance the Lewis acidity of Co sites. The presence of vacancies strengthens the interaction between Pt and Co through bridged oxygen atoms, subtly redistributing charge and increasing the acidity of Co centers. These Lewis acidic Co sites preferentially coordinate with OH$^-$ species, leading to preferential OH$^-$ adsorption on Co rather than Pt. Once the surface is covered by

OH⁻, steric and electrostatic effects repel Cl⁻ ions, thereby lowering their surface affinity and mitigating chloride induced poisoning under simulated seawater conditions. Guided by this understanding, the electrochemical behavior of Pt–CoO$_x$ was further investigated in alkaline electrolytes containing Cl⁻. As shown in Fig. S39, corrosion polarization measurements demonstrate that Pt–CoO$_x$ exhibits a much lower corrosion current density (-4.058 mA cm^{-2}) and a higher corrosion potential (0.863 V) than Pt–CoO, indicating that oxygen vacancies not only enhance catalytic activity but also improve seawater electrolysis stability.[41,42] Given that the chloride concentration in seawater gradually increases during electrolysis, the catalytic performance of Pt–CoO$_x$ and Pt–CoO was further evaluated under electrolytes of varying salinity (Fig. 5a). Pt–CoO$_x$ maintains excellent catalytic stability even in high salt environments, whereas the chloride sensitive Pt–CoO suffers from severe performance degradation due to Cl⁻ poisoning.[43,44] To further assess its practical potential, HER performance was tested in natural seawater. As shown in Fig. 5b, Pt–CoO$_x$ exhibits higher catalytic activity than Pt–CoO, requiring only 463 mV to reach a current density of 150 mA cm^{-2}, compared with 485 mV for Pt–CoO. Multiple electrochemical parameters corroborate this enhancement (Fig. 5c and S40). First, its smaller Tafel slope

of 69.89 mV dec^{-1} indicates that oxygen vacancies expose more active sites and accelerate HER kinetics. Moreover, Pt–CoO$_x$ shows a double layer capacitance (C_{dl}) of 5.87 mF cm^{-2} nearly three times that of Pt–CoO (2.09 mF cm^{-2}) corresponding to an electrochemically active surface area (ECSA) approximately 2.8 times larger. Subsequently, at 0.5 V, the TOF of Pt–CoO$_x$ reaches 1.35 s^{-1}, which is significantly higher than that of Pt–CoO of 0.78 s^{-1}, indicating a higher reaction efficiency per active site. Meanwhile electrochemical impedance spectroscopy analysis shows that the charge transfer resistance of Pt–CoO$_x$ is only 1.48 Ω compared with 2.41 Ω for Pt–CoO (Fig. S41), demonstrating that the introduction of oxygen vacancies effectively reduces interfacial charge transfer resistance and further promotes the reaction kinetics. Moreover, the corrosion resistance of both catalysts was further evaluated in real seawater (Fig. 5d). Pt–CoO$_x$ exhibits a higher corrosion potential and a lower corrosion current than Pt–CoO, confirming that oxygen vacancies substantially strengthen its structural robustness. During seawater electrolysis, local pH elevation near the cathode can cause Ca^{2+} and Mg^{2+} to form hydroxide precipitates that block active sites and hinder hydrogen evolution. Long term electrolysis at 50 mA cm^{-2} (Fig. 5e) reveals that Pt–CoO$_x$ accumulates far fewer white deposits than Pt–CoO or Ni foam (NF),
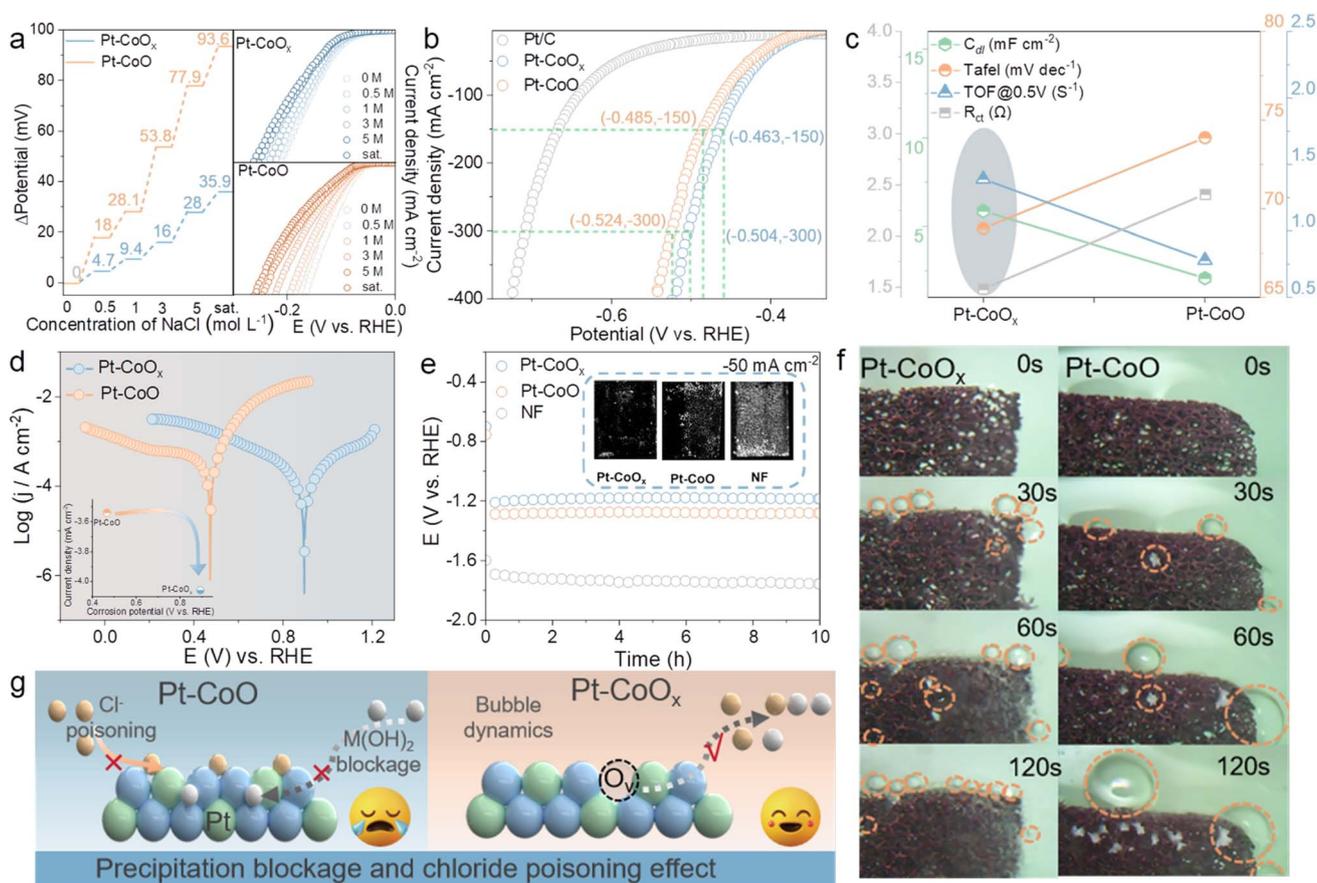

Fig. 5 (a) Overpotentials of Pt–CoO$_x$ and Pt–CoO at different Cl⁻ concentrations. (b) LSV curves in natural seawater. (c) C_{dl}, Tafel, TOF, and R_{ct} of the samples. (d) Corrosion polarization curves of the samples in natural seawater. (e) Chronopotentiometric curves of Pt–CoO$_x$ and Pt–CoO at different current densities (inset shows corresponding optical photographs). (f) Bubble dynamics experimental diagram. (g) Schematic illustration of anti-poisoning and anti-precipitation properties of the samples in natural seawater.

demonstrating superior resistance to scaling. Notably, we also performed XRD analysis (Fig. S42) on the precipitates collected from the electrolyte and identified them as $Mg(OH)_2$, which is commonly regarded as a high value-added product, thereby to some extent expanding the application prospects of this system for the co-utilization of products during seawater electrolysis. To elucidate this effect, gas bubble dynamics were visualized (Fig. 5f).[45] The Pt–CoO_x electrode generates fine bubbles that detach rapidly from the surface, while Pt–CoO produces larger bubbles with slower release. The faster bubble detachment on Pt–CoO_x provides continuous micro agitation that prevents Ca/Mg hydroxide deposition, whereas bubble retention on Pt–CoO facilitates salt layer formation. Importantly, the stable Pt–O–Co bridge oxygen bond formed in the presence of vacancies modulates interfacial water orientation and polarization, optimizing the local hydrogen bond network. Combined with *in situ* Raman results, Pt–CoO_x exhibits a higher fraction of free water and a more relaxed hydrogen bond network, which lowers the nucleation and detachment barriers of bubbles, leading to smaller, more uniformly released bubbles and significantly less surface contamination. In summary, the synergistic regulation of oxygen vacancies and Pt–O–Co bridging structures enhances the Lewis acidity of Co sites and reconstructs the interfacial water configuration. These effects enable Pt–CoO_x to dynamically repel Cl^- adsorption and promote efficient bubble release, thereby simultaneously suppressing chloride corrosion and salt deposition induced deactivation, resulting in superior catalytic stability and HER durability in seawater (Fig. 5g).

Conclusion

In summary, we have developed a Pt–CoO_x catalyst featuring an asymmetric Pt–O–Co bridging structure with rich oxygen vacancies, where the introduction of oxygen vacancies enables synergistic modulation of interfacial electronic states and the reaction microenvironment. This structural configuration optimizes the thermodynamics of hydrogen adsorption and enhances the Lewis acidity of Co sites, promoting preferential OH^- adsorption while suppressing Cl^- competition, thereby preventing Pt site poisoning. Benefiting from these electronic and structural advantages, Pt–CoO_x achieves overpotentials of only 160.22 and 207.22 mV at 500 and 1000 mA cm^{-2}, respectively, and maintains stable operation for 100 hours at 500 mA cm^{-2} in alkaline seawater. Moreover, oxygen vacancy induced interfacial water reorganization reduces the bubble detachment barrier, facilitating rapid bubble release and effectively mitigating Ca/Mg^{2+} precipitation. This work offers a new design paradigm for constructing highly efficient and corrosion resistant catalysts for seawater hydrogen evolution.

Author contributions

Mengyue Gao: investigation, data curation, conceptualization, formal analysis, validation, writing – original draft. Junfeng Qin: conceptualization, writing – review & editing, supervision. Rui Zhang: data curation, conceptualization. Xu Liu: formal analysis, data curation. Yuxin Liu, Yuxin Zhang: supervision, validation. Long Song, Jingyi Xie: supervision, validation, conceptualization. Jingqi Chi, Xiaobin Liu: supervision, validation, funding acquisition. Lei Wang: writing – review & editing, funding acquisition, supervision.

Conflicts of interest

The authors declare that they have no known competing financial interests or personal relationships that could have appeared to influence the work reported in this paper.

Data availability

The data that support the findings of this study are available from the corresponding author upon reasonable request.

Supplementary information: experimental procedures, characterization data of the materials (SEM, XRD, XPS, ICP-OES) and computational details. See DOI: https://doi.org/10.1039/d5sc09928e.

Acknowledgements

References

1 M. Wang and J. Luo, *eScience*, 2023, **3**, 100155.

2 R. Ding, J. Chen, Y. Chen, J. Liu, Y. Bando and X. Wang, *Chem. Soc. Rev.*, 2024, **53**, 11390–11461.

3 L. Song, L. Guo, J. Mao, Z. Li, J. Zhu, J. Lai, J. Chi and L. Wang, *ACS Catal.*, 2024, **14**, 6981–6991.

4 X.-L. Zhang, P.-C. Yu, S.-P. Sun, L. Shi, P.-P. Yang, Z.-Z. Wu, L.-P. Chi, Y.-R. Zheng and M.-R. Gao, *Nat. Commun.*, 2024, **15**, 9462.

5 Y. Liu, Y. Wang, P. Fornasiero, G. Tian, P. Strasser and X. Yang, *Angew. Chem., Int. Ed.*, 2024, **63**, e202412087.

6 C. Zhao, Z. Ding, K. Zhang, Z. Du, H. Fang, L. Chen, H. Jiang, M. Wang and M. Wu, *Nano-Micro Lett.*, 2025, **17**, 113.

7 M. J. S. Mohamed, M. A. Gondal, M. Hassan, M. A. Almessiere, A. A. Tahir and A. Roy, *ACS Omega*, 2023, **8**, 33332–33341.

8 Y. Sun, W. Sun, L. Chen, A. Meng, G. Li, L. Wang, J. Huang, A. Song, Z. Zhang and Z. Li, *Nano Res.*, 2023, **16**, 228–238.

9 M. Pan, X. Cui, Q. Jing, H. Duan, F. Ouyang and R. Wu, *RSC Adv.*, 2025, **15**, 19079–19087.

10 S. Xu, J. Cen, G. Yang, L. Si, X. Xiao and H. Liu, *Chem. Res. Chin. Univ.*, 2024, **40**, 1106–1115.

11 M. Ning, Y. Wang, L. Wu, L. Yang, Z. Chen, S. Song, Y. Yao, J. Bao, S. Chen and Z. Ren, *Nano-Micro Lett.*, 2023, **15**, 157.

12 L. Guo, Q. Yu, X. Zhai, J. Chi, T. Cui, Y. Zhang, J. Lai and L. Wang, *Nano Res.*, 2022, **15**, 8846–8856.

13 H. Ma, S. Wu, M. Li, Z. Xiao, X. Liu, J. Chi, J. Lai and L. Wang, *Green Chem.*, 2025, **27**, 12909–12945.

14 Q. Li, Q. Xu, Z. Pei, Z. Zhang, W. Xu, J. Mao, Q. Shang, Y. Ni, Y. Chen, Y. Chen, X. Liu, X. Li, Q. Zhang and N. Yang, *Adv. Energy Mater.*, 2025, 2500815.

15 Y. Han, M. A. Sinnwell, S. J. Teat, M. L. Sushko, M. E. Bowden, Q. R. S. Miller, H. T. Schaef, L. Liu, Z. Nie, J. Liu and P. K. Thallapally, *Adv. Sci.*, 2019, **6**, 1802056.

16 H. Mao, X. Liu, T. Cui, J. Tang, Z. Su, J. Chi, Y. Chai, Z. Wu and L. Wang, *Angew. Chem., Int. Ed.*, 2025, **64**, e202511867.

17 T. Xu, D. Jiao, L. Zhang, H. Zhang, L. Zheng, D. J. Singh, J. Zhao, W. Zheng and X. Cui, *Appl. Catal., B*, 2022, **316**, 121686.

18 X. Wang, X. Li, J. Mu, S. Fan, X. Chen, L. Wang, Z. Yin, M. Tadé and S. Liu, *ACS Appl. Mater. Interfaces*, 2019, **11**, 41988–41999.

19 X. Liao, H. Cui, H. Luo, Y. Lv and P. Liu, *Chem. Eng. J.*, 2025, **509**, 161231.

20 C.-H. Liu, K.-Y. Hsiang, Z.-X. Li, F.-S. Chang, Z.-F. Lou, J.-Y. Lee, C. W. Liu, P. Su, T.-H. Hou and M.-H. Lee, *ACS Appl. Mater. Interfaces*, 2025, **17**, 14342–14349.

21 Y. Fang, H. Li, Q. Zhang, C. Wang, J. Xu, H. Shen, J. Yang, C. Pan, Y. Zhu, Z. Luo and Y. Guo, *Environ. Sci. Technol.*, 2022, **56**, 3245–3257.

22 L. Ma, Y. Wang, Y. Chen, R. Han, D. Xu, D. Jiao, D. Wang and X. Yang, *Adv. Funct. Mater.*, 2025, **35**(35), 2503358.

23 Z. Teng, C. Liu, R. Zhang, X. Liu, S. Wang, J. Zhu, J. Chi, Z. Wu, X. Liu and L. Wang, *ACS Nano*, 2025, **19**, 30930–30940.

24 X. Liu, X. Liu, C. Li, B. Yang and L. Wang, *Chin. J. Catal.*, 2023, **45**, 27–87.

25 Y. Xia, J. Chi, J. Tang, X. Liu, Z. Xiao, J. Lai and L. Wang, *Chin. J. Catal.*, 2024, **66**, 110–138.

26 X. Yang, H. Shen, X. Xiao, Z. Li, H. Liang, S. Chen, Y. Sun, B. Jiang, G. Wen, S. Wang and L. Zhang, *Adv. Mater.*, 2025, **37**, 2416658.

27 M. Li, C. Liu, Z. Teng, R. Zhang, X. Liu, J. Zhu, X. Liu, Z. Wu, Y. Chai, J. Chi and L. Wang, *Adv. Funct. Mater.*, 2025, **35**(52), e14517.

28 Z. Li, X. Liu, Q. Yu, X. Qu, J. Wan, Z. Xiao, J. Chi and L. Wang, *Chin. J. Catal.*, 2024, **63**, 33–60.

29 W. Yan, Y. Mou, M. Li, K. Ma, Z. Xu, T. Lu, H. Du, C. Wang, H. Sun, L. Chen, Y. Tang, Y. Wang and G. Fu, *Adv. Mater.*, 2025, **37**, 2506936.

30 X. Chen, X.-T. Wang, J.-B. Le, S.-M. Li, X. Wang, Y.-J. Zhang, P. Radjenovic, Y. Zhao, Y.-H. Wang, X.-M. Lin, J.-C. Dong and J.-F. Li, *Nat. Commun.*, 2023, **14**, 5289.

31 S. Shen, Q. Li, H. Zhang, D. Yang, J. Gong, L. Gu, T. Gao and W. Zhong, *Adv. Mater.*, 2025, **37**(15), 2500595.

32 M. Xu, Y. Kang, L. Wang, Y. Zhang, G. Jiang, Y. Cai, Y. Tu, Q. Zhao, J. Chi, W. Song, H. Yu, J. Hu, W. Liu, R. Huang, L. Yu, J. Lu, X. Bao and D. Deng, *Joule*, 2025, 101968.

33 K. Huang, R. Li, H. Qi, S. Yang, S. An, C. Lian, Q. Xu, H. Liu and J. Hu, *ACS Catal.*, 2024, **14**, 8889–8898.

34 S. Chen, X. Li, C. Kao, T. Luo, K. Chen, J. Fu, C. Ma, H. Li, M. Li, T. Chan and M. Liu, *Angew. Chem., Int. Ed.*, 2022, **61**, e202206233.

35 C. Wang, P. Li, D. Chen, R. Zhang, L. Wang and L. Zong, *Chem. Res. Chin. Univ.*, 2024, **40**, 462–474.

36 J. Zhou, M. Wen, R. Huang, Q. Wu, Y. Luo, Y. Tian, G. Wei and Y. Fu, *Energy Environ. Sci.*, 2023, **16**, 2611–2620.

37 C. Feng, Q. Gao, G. Xiong, Y. Chen, Y. Pan, Z. Fei, Y. Li, Y. Lu, C. Liu and Y. Liu, *Appl. Catal., B*, 2022, **304**, 121005.

38 Z. Li, H. Mao, X. Liu, J. Wan, J. Chi, S. Huang, Q. Lv, Z. Wu and L. Wang, *ACS Nano*, 2025, **19**, 9070–9080.

39 C. Chen, Y. Wang, J. Li, F. Tian, W. Chen, C. Feng, Y. Pan and Y. Liu, *Appl. Catal., B*, 2023, **338**, 123086.

40 T. Xiang, D. Dai, X. Li, D. Liu, C. Feng, P. Dai, L. Li, X. Gu and Y. Liu, *Appl. Catal., B*, 2024, **348**, 123841.

41 X. Kang, F. Yang, Z. Zhang, H. Liu, S. Ge, S. Hu, S. Li, Y. Luo, Q. Yu, Z. Liu, Q. Wang, W. Ren, C. Sun, H.-M. Cheng and B. Liu, *Nat. Commun.*, 2023, **14**, 3607.

42 W. Hao, X. Ma, L. Wang, Y. Guo, Q. Bi, J. Fan, H. Li and G. Li, *Adv. Energy Mater.*, 2025, **15**, 2403009.

43 X. Xu, Y. Lu, J. Shi, X. Hao, Z. Ma, K. Yang, T. Zhang, C. Li, D. Zhang, X. Huang and Y. He, *Nat. Commun.*, 2023, **14**, 7708.

44 Q. Yu, Y. Fu, Z. Liu, X. Liu, L. Guo, T. Wang, J. Chi, Z. Wu and L. Wang, *Appl. Catal., B*, 2025, **361**, 124598.

45 T. Li, Z. Zheng, Z. Chen, M. Zhang, Z. Liu, H. Chen, X. Xiao, S. Wang, H. Qu, Q. Fu, L. Liu, M. Zhou, B. Wang and G. Zhou, *Energy Environ. Sci.*, 2025, **18**, 4996–5008.